Sociedad Mexicana de Ingeniería Mecánica
Fecha de recepción: 15-10-2016
Fecha de aceptación: 23-01-2017

INGENIERÍA MECÁNICA
TECNOLOGÍA Y DESARROLLO
Vol. 5 No. 6 (2017) 459 - 473

Progressive failure analysis of wind turbine blades under stochastic fatigue loads

[1]Diego Cárdenas, [2,*]Oliver Probst, [1]Hugo Elizalde
Tecnológico de Monterrey, Escuela de Ingeniería y Ciencias
[1]Calle del Puente 222, Col. Ejidos de Huipulco, Tlalpan, México, DF, CP14380, Mexico.
[2]Eugenio Garza Sada 2501 Sur, Monterrey, NL, Mexico, CP 64849.
*Corresponding author: oprobst@itesm.mx

Resumen

Se presenta una novedosa metodología para el análisis de la progresión del daño por fatiga en aspas de aerogeneradores sujetas a cargas de viento estocásticas. El modelo representa una extensión de trabajos previos sobre la progresión de daño por fatiga en vigas de pared delgada hechas con materiales compuestos al incorporar capacidades de modelamiento aeroelásticas y el efecto de cargas de viento estocásticas. La novedad principal de la propuesta consiste en su capacidad de conducir un análisis automatizable al contar con un modelo computacionalmente esbelto que a pesar de su eficiencia computacional permite el seguimiento detallado de la evolución de las propiedades de los materiales con alta resolución espacial, incluyendo la posibilidad de analizar capa por capa. Un caso de estudio numérico basado en el aspa de una pequeña turbina eólica construida con materiales compuestos y sujeta a cargas de viento estocásticas durante 20 años ha sido simulado. Se muestran e interpretan mapas de daño detallados indicando la ubicación y el tipo de daño y se relacionan dichos mapas con gráficas de la evolución global del daño por tipo de mecanismo de degradación, además de demostrarse el efecto sobre las propiedades elásticas globales. También se discute el efecto del daño por fatiga sobre el desempeño aerodinámico. Aplicaciones de la innovación incluyen el diseño de estructuras más livianas y más económicas, además de la opción de un diseño para sitios específicos.

Abstract

A novel methodology for integrated progressive fatigue failure analysis in wind turbines blades subjected to stochastic wind loads is presented and demonstrated. The model extends previous work on fatigue failure progression and composite thin-walled beams by incorporating aeroelastic modeling capabilities and the effect of stochastic wind loads. The main novelty of the approach lies with its ability to conduct an automated computationally lean assessment with full information on layer- and position-resolved damage in the walls of the blade. A numerical test case of a small wind turbine blade built from composite material and subjected to simulated stochastic wind loads was modeled for a 20-year period. Detailed spatial maps of damage localization and the associated failure type are shown and related to the evolution of the global elastic properties of the blade. The effect of fatigue damage on the aerodynamic performance is demonstrated. Applications of the novel approach include the design of lighter and less expensive, as well as site-specific turbine blades.

Palabras clave:
Aspas de aerogeneradores; fatiga; vigas de pared delgada; carga de viento estocásticas; propagación de daño

Nomenclature

The following is a list of the major symbols used in the text:

C_p	Aerodynamic power coefficient
$f_U(\bar{U}_{\infty,10})$	Normalized histogram of 10-min average wind speed values
f_σ^{ij}	Normalized bivariate histogram of (σ_a, σ_m) values for a given wind speed class
$\overline{f_\sigma^{ij}}$	Normalized bivariate histogram of (σ_a, σ_m) values averaged over wind speed classes
n	Number of fatigue cycles for a given (σ_a, σ_m) pair
$n_{eq}^{(\kappa)}$	Equivalent number of cycles after k previous fatigue blocks
N_f	Number of fatigue cycles to failure for a given (σ_a, σ_m) pair
σ_z	Linear stress along the blade axis
σ_{sz}	Shear stress in the plane of the shell material
σ_{11}	Linear stress along the local fiber axis
σ_{22}	Linear stress perpendicular to the local fiber axis

Keywords:
Wind turbine blades; fatigue; thin-walled beam; stochastic wind loads; damage propagation

σ_{12}	Shear stress in the local material frame of reference
$\sigma_{\max}$	Maximum stress during a fatigue cycle in either of the material directions
σ_a	Stress amplitude of a fatigue cycle
σ_m	Average stress of a fatigue cycle
(r, s, z)	Local cylindrical coordinates of blade section
S_r	Residual material strength for either degree of freedom at a given location & stress level
S_{11T}	Local residual tensile strength in along-the-fiber direction
S_{11C}	Local residual compressive strength in along-the-fiber direction
S_{22T}	Local residual tensile strength in the direction perpendicular to the fiber
S_{22C}	Local residual compressive strength in the direction perpendicular to the fiber
S_{12}	Local residual shear strength
u_{flap}	Flapwise (perpendicular to the rotor plane) displacement of a given blade section

u_{edge}	Edgewise (in the rotor plane) displacement of a given blade section
$U_{\infty}(t)$	Free-stream wind speed time series without specified gust value
$U_{\infty,c}(t)$	Free-stream wind speed time series with gust control
$v_{\max}$	Gust value of a given wind speed time series
$v_{\min}$	Anti-gust value of a given wind speed time series

Introduction

Wind turbine blades are generally built from thin-walled composite structures [1], given their high strength/weight ratio and the versatility to suit specific aerodynamic and structural requirements. While blades are occasionally exposed to extreme load conditions, which have to be assessed in the design phase in order to certify the suitability of the blades for a given wind class [2], they are also continuously subjected to a spectrum of low and moderate fatigue loads which accumulate damage over the lifetime of the rotor. The continuous degradation of the blade structure represents a significant challenge as the structural properties continuously evolve over a wide range of time scales, ranging from seconds to about 20 years, thereby spanning about nine orders of magnitude [1]. Generally, a probabilistic approach is pursued for fatigue design of wind turbine blades [3]. While such an approach is conveniently simple and computationally efficient, it is not suited for a detailed assessment with insights into region- or layer-specific damage initiation and propagation, failure-interaction between layers due to changes in load carrying capacity, and changes in material properties over time [3]. Consequently, substantial safety factors have to be applied to compensate for the high uncertainty, resulting in heavier and more costly turbine blades.

In order to address these shortcomings some efforts have been made to model failure propagation in wind turbine blades under realistic conditions and allow for a progressive accumulation of damage. Shokrieh & Rafiee [4] proposed a progressive fatigue damage model which incorporates both a gradual reduction of the stiffness and strength moduli as a consequence of materials degradation due to fatigue as well as conditions for sudden (i.e. static) failure, and applied it to the assessment of the fatigue life of a wind turbine blade. Spatial tracking of damage in composite materials has been studied by several groups in recent years, with the focus being on progressive failure analysis of simple geometries, as opposed to a detailed modeling of a complex structure such as a wind turbine blade. Lee et al. [5] conducted a progressive failure analysis for through hole-loaded composite samples and static loads, implementing an ABAQUS subroutine to iteratively modify the finite-element (FE) stiffness matrix as a consequence of materials degradation. Nishikov et al. [6] investigated fatigue-induced damage in composites due to matrix cracks and delamination, providing damage maps qualitatively comparable to experiments. Cárdenas et al. [7] conducted a damage propagation analysis for a complex helicopter blade previously studied in [8], comparing the results of their damage progression software based on a Librescu-type [9] thin-walled beam (TWB) model and a failure progression algorithm with those obtained with the commercial software suite GENOA [10]. An agreement within a few percent was obtained for the global damage growth as a function of load between the TWB and the more complex shell-based model. Also, the spatial propagation patterns were found to be very similar. Cárdenas et al. [11] presented a dynamical version of their previous work allowing for damage propagation in wind turbine blades to be modelled under realistic instantaneous loads, although fatigue loads were not considered at that time. A TWB-based damage progression model for the case of fatigue loads was recently presented by Rivera et al. [12] which drew on progress on thin-walled structures [8], [9], [11], progressive failure analysis [13], [14], and fatigue damage and degradation modeling in composites [15], [16], [17]. Recent work in fatigue modeling of wind turbine blades includes the papers by Jang et al. [18] and Montesano et al. [19]. Jang et al. presented a modular approach for estimating fatigue life in different wind climates by combining stochastic wind generation, Blade Element Momentum (BEM) modeling of aerodynamic forces using the open source code PROPID, FE calculation of the (root) bending moments using the commercial software ABAQUS, and empirical stress vs. fatigue life relationships. Montesano et al. developed a multi-scale damage model and incorporated it into the commercial FE package ANSYS and demonstrated the capability for spatial tracking of the ply crack density for quasi-static and fatigue loading.

In the present work a novel methodology for modeling fatigue-induced damage in complex composite structures such as wind turbine blades subjected to stochastic wind loads is proposed. This new contribution extends previous work by these authors on aeroelastic modeling, fatigue failure progression and thin-walled beam modeling [12] by fully incorporating aeroelastic capabilities and the effect of stochastic wind loads. Some of the advantages of the new methodology over other approaches include the following: (1) Fatigue damage is assessed at each layer of the entire blade's geometry, not only at critical regions (i.e. the root). (2) The model is fully integrated and does not require manual data exchange between different tools. (3) Coupled structural-aerodynamic analysis is performed via validated reduced-order models (i.e. TWB and BEM, respectively), allowing for fast execution and consequently long modeling time horizons. (4) Fatigue modeling is not limited to fixed amplitudes, thus stochastic loads arising from realistic wind resource profiles can be evaluated conveniently. The approach is currently limited to the use of empirical fatigue damage and degradation rules which are well validated on a coupon level but may have accuracy limitations when it comes to assess complex stress states; these issues, as well as the comprehensive experimental validation that any numerical model requires, will be addressed in follow-up work.

The paper has the following structure: first, the fundamentals of TWB modeling and its application to damage propagation are briefly reviewed. The methodology of the new contributions of the present work is then described in some detail as well as the study case designed to illustrate the methodology. We then present the results of the study case and conclude the paper with an outlook for future work and some recommendations.

Methodology

Thin-walled beam (TWB) and fatigue damage propagation model

The present formulation of the structural model is based on a thin-walled beam approach pioneered by Librescu and others [9], [14], providing semi-analytical expressions for the stiffness tensor of arbitrary cross-sections. A TWB model reduces all geometric and material information of the shell material to a single axial line with a few degrees of freedom, while being capable of recovering strain and stress information with enough detail at each coordinate/layer of the shell material, based on the knowledge of the global displacements alone. Once the TWB displacement field has been calculated, the strain field is recovered as follows:

$$\begin{aligned}\epsilon_{zz} = \epsilon^{0}_{zz} &+ \left[y(s) - n\cos\alpha(s)\right]\kappa_x + \\ &+ \left[x(s) + n\sin\alpha(s)\right]\kappa y + \left[\omega(s) - nq(s)\right]\kappa\omega\end{aligned} \tag{1}$$

$$\gamma_{sz} = \bar{\gamma}_{sz} + 2n\kappa_{xy}, \tag{2}$$

where ϵ_{zz} is the linear axial strain along the blade axis (*z*), and γ_{sz} is the shear strain in the plane of the shell material (*s,z*). *x, y, z* are the global Cartesian coordinates aligned to the flapwise, edgewise and axial motions, respectively. *n,s* is an auxiliary coordinate system representing the normal and tangential coordinates of an arbitrary point located in the shell and with its origin located at an arbitrary point on the mid-surface of the cross-section. κ_x, κ_y, κ_{xy}, κ_ω are curvatures in the *xz* plane (flapwise bending), *yz* plane (edgewise bending), rate of torsion, and curvature of torsion, respectively. ϵ^0_{zz} is the global axial strain of the representative axial line, and barred variables (i.e. $\bar{\gamma}_{sz}$,$\bar{\epsilon}_{zz}$) refer to quantities defined at the mid-surface. The shear strain $\bar{\gamma}_{sz}$ contains coupling terms between axial and shear deformation, following the formulation of Zhang & Wang [21].

Stress fields can be defined at each lamina *k*, obeying the following constitutive law:

$$\begin{Bmatrix}\sigma_z\\ \sigma_{sz}\end{Bmatrix} = \begin{bmatrix}\bar{Q}^*_{11} & \bar{Q}^*_{16}\\ \bar{Q}^*_{16} & \bar{Q}^*_{66}\end{bmatrix}\begin{Bmatrix}\varepsilon_z\\ \gamma_{sz}\end{Bmatrix}, \tag{3}$$

where the $\bar{Q}^*_{ij}$ are stiffness coefficients defined in a material (i.e. local) frame, then reduced from a 3D orthotropic law to plane stress conditions, and finally transformed to global (i.e. analysis) coordinates. The resultant global stress field must be transformed back to material coordinates to allow for the evaluation of failure criteria at each layer:

$$\begin{bmatrix}\sigma_{11} & \sigma_{12}\\ \sigma_{21} & \sigma_{22}\end{bmatrix}_{\kappa} = [T]\begin{Bmatrix}\sigma_z\\ \sigma_{sz}\end{Bmatrix}_{\kappa}[T]^T, \tag{4}$$

where subscripts 1, 2 correspond to directions along- and perpendicular to the fiber, respectively, and [*T*] collects the director cosines between global and material frames for each layer.

The fatigue damage model used in the present work builds on an approach described in Rivera et al. [12], Shokrieh [16], and Shokrieh & Lessard [13]. This approach is based on three components: 1) calculation of the stress field throughout the structure, 2) rules for *sudden* damage of the material and 3) rules for *gradual degradation* of materials properties. *Sudden* material damage occurs if one of five failure criteria, proposed by Hashin [24], is met. Each of these criteria represents a particular failure mode: fiber tension (subindex 11T), fiber compression (11C), matrix tension (22T), matrix compression (22C), and shear (12). *Gradual* degradation of the material is modelled by parametric expressions for the residual strength S_r and residual stiffness E_r, respectively, as functions of the number of load cycles *n* at a given stress amplitude $\sigma_{\max}$ (assumed constant in the original formulation by Shokrie [16]). The extension to variable fatigue amplitudes proposed in the current work will be described further below. The equation for the residual strength reads [16], [22]:

$$\frac{S_r - \sigma_{\max}}{S_0 - \sigma_{\max}} = \left[1 - \left(\frac{\log n - \log 0.25}{\log N_f - \log 0.25}\right)^{\beta}\right]^{\frac{1}{\alpha}} \tag{5}$$

S_0 is the initial material strength, N_f the number of cycles to fatigue failure, and α and β are certain material-specific exponents obtained experimentally. The values of α and β determined by [16] were used throughout the present work, see Table 1; a separate equation of the type (5) applies to each of the five failure modes. The gradual degradation rule for the residual stiffness E_r can be cast into an analogous form with exponents λ and γ [16]. While equation (5) appears to depend only on the maximum stress $\sigma_{\max}$, the mean stress acting on a given material segment is implicitly accounted for in the number of cycles to failure N_f. Following [16], [4] N_f is calculated from the model introduced by Adam et al. [23]. For a given lamina, a different value of N_f is calculated for each of the three in-plane material directions (11, 22, 12):

$$A_{ij} + B_{ij}\log\left(N_f\right)_{ij} = u_{ij}, \tag{6}$$

where the sub-indices i,j range from 1 to 2 to represent a certain material direction (11, 22, 12), and

$$u_{ii} = \frac{\ln\left(a_{ii}/1.06\right)}{\ln\left[\left(1-q_{ii}\right)\left(c_{ii}+q_{ii}\right)\right]} \qquad \left(i=1,2\right) \tag{7}$$

$$u_{12} = \log\left(\frac{\ln\left(a_{12}/1.06\right)}{\ln\left[\left(1-q_{12}\right)\left(c_{12}+q_{12}\right)\right]}\right) \tag{8}$$

a_{ij}, q_{ij}, and c_{ij} are calculated as follows:

$$\left(q_{ij}, a_{ij}, c_{ij}\right) = N_{ij}\left(\sigma_{ij}^{(m)}, \sigma_{ij}^{(a)}, \tilde{S}_{ij}\right), \tag{9}$$

where $\tilde{S}_{11} = S_{11,c}$, $\tilde{S}_{22} = S_{22,t}$, $\tilde{S}_{12} = S_{12}$, $N_{11} = 1/S_{11,t}$, $N_{22} = 1/S_{22,c}$, and $N_{12}=1/S_{12}$. $\sigma_{ij}^{(m)}$ and $\sigma_{ij}^{(a)}$ are the mean and the amplitude of the alternating stress signal, respectively, i.e.

$$\sigma_{ij}^{(m,a)} = \frac{1}{2}\left(\sigma_{ij}^{(\max)} \pm \sigma_{ij}^{(\min)}\right) \tag{10}$$

Wind speed time series generation

The integrated modeling process of the present methodology starts with the generation of the stochastic free-stream wind speed time series for a given time interval (typically 10 mins) according to [25]

$$U_\infty\left(t\right) = \bar{U}_\infty + \sum_{i=1}^{N} A_i \cos\left(2\pi\tilde{n}_i t + \varphi_i\right), \tag{11}$$

where the amplitudes A_i and phases φ_i are drawn from a normal distribution with variance ρ_A^2 and a uniform distribution, respectively, and the frequencies $\tilde{n}_i$ are generated based on the Fourier transform of the autocorrelation function (or power density spectrum, PDS) $S_U(\tilde{n})/\rho_v^2$ which should be consistent with typical wind turbulence; N is the number of Fourier components. In the present case the Kaimal PDS was chosen to model turbulence:

$$\frac{S_U\left(\tilde{n}\right)\tilde{n}}{\rho_\upsilon^2} = \frac{4\tilde{n}L_1/\bar{U}_\infty}{\left(1+6\tilde{n}L_1/\bar{U}_\infty\right)^{5/3}}, \tag{12}$$

where L_1 is a characteristic length of the order of 150-200m. $\bar{U}_\infty$ is the mean of the wind speed of the given time interval, and ρ_v^2 its variance, where $\rho_v^2 = N\rho_A^2/2$. The mean wind speed and the variance for 10-min intervals are typically available from data logger records. The signal (11) can be modified to account for the measured values of the gust $v_{\max}$ (and anti-gust) in the interval by [25]

$$U_{\infty,c}\left(t\right) = U_\infty\left(t\right) + \left(\upsilon_{\max} - U_\infty\left(t_0\right)\right)\kappa\left(t-t_0\right) + \frac{\dot{U}_\infty\left(t_0\right)\dot{\kappa}\left(t-t_0\right)}{-\ddot{\kappa}\left(0\right)}, \tag{13}$$

where $\kappa(\tau)$ is the autocorrelation function of the original signal, and t_0 is the moment of time where the largest wind speed in the original time series occurred. As usual, dots refer to time derivatives.

Calculation of aerodynamic loads and aeroelastic coupling

Quasi-stationary flow conditions are assumed at the wind turbine blade, allowing Blade Element Momentum (BEM) theory to be used for the calculation of the aerodynamic loads on the blade. Corrections arising from unsteady flow will be included in future versions of the model. Using the BEM approach the forces and moments on a beam segment dz can be calculated as follows:

$$\left(\mathrm{d}L, \mathrm{d}D, \mathrm{d}M\right) = \frac{1}{2}\rho c\left(r\right)V_{tot}^2\left(C_L, C_D, C_M\right)\mathrm{d}z, \tag{14}$$

where dL and dD are the lift and drag force on the beam segment dz, respectively, and dM is the moment around the aerodynamic center of the local airfoil, usually located at about 25% of the local chord. If the aerodynamic center of a given section airfoils is not at the blade axis an additional moment arises from the leverage of the lift and drag forces on the section, giving rise to the total pitching moment of the section. V_{tot} is the total effective wind speed at the section obtained from the inflow speed $U_\infty(z)$, the rotational speed Ωz of the section located at a distance z along the blade axis, and the airfoil induced axial and rotational components $-a(z)U_\infty$ and $a'(z)\Omega z$, respectively. $a(z)$ and $a'(z)$ are calculated self-consistently from the balances of linear and angular momentum of airflow and rotor blades at annuli between z and $z + dz$, where the formulation described in Martínez et al. [26] has been used in the present work.

U_∞ is generally assumed to be constant over the swept rotor area, which is often a good approximation, especially for smaller rotors such as the one studied in the present work. For larger swept areas, however, the wind field ceases to be coherent and there is a significant dependence of the wind speed time series on the location along the blade axis because of rotational sampling arises. Also, the sampling of the vertical wind speed profile by the rotating blade introduces a significant departure from the constancy of U_∞, which is why the model introduced in the present considers the possibility of a radial variation of U_∞.

Aeroelastic coupling is achieved by incorporating the local rotation of the section airfoil at a blade axial position z determined from

$$\left[M\right]\left\{\ddot{u}\right\} + \left[C\right]\left\{\dot{u}\right\} + \left[K\right]\left\{u\right\} = \left\{f\right\}, \tag{15}$$

where

$$\left\{u\right\} = \left(U, V, W, \varphi\right) \tag{16}$$

and

$$\{f\} = \left(f_{\text{flap}}, f_{\text{edge}}, f_{\text{span}}, M_{\text{torsion}}\right). \qquad (17)$$

[M], [C], and [K] are the mass, hysteretic damping, and stiffness matrices of a given blade segment, respectively, {*u*} groups the degrees of freedom, and {*f*} represents the local loads acting on the blade segment due to aerodynamic forces (equation (14)). Only one rotational degree of freedom (i.e. torsion around the blade's main axis) is included in the current formulation as an Euler formalism has been used, though generalization to Timoshenko is straightforward. The implementation and solution of the above equations is based on an isogeometric formulation (as opposed to a standard finite-element model) which will be reported elsewhere. The local angle of attack of the section airfoil can now be calculated from

$$\alpha(z) = \phi(z) - \beta'(z) = \phi(z) - \beta(z) - \varphi(z), \qquad (18)$$

where $\phi(z)$ is the local flow angle as determined by BEM and $\beta(z)$ is the local design airfoil pitch angle, both as measured from the plane of rotation; $\varphi(z)$ is the rotation angle of the local section as determined by the TWB model. $\phi(z)$ and $\varphi(z)$ are calculated self-consistently from the coupled TWB-BEM model.

A graphical representation of the modeling process based on the elements described above is given in Figure 1.

Fatigue degradation and damage modeling

The coupling between the structural and aerodynamic behavior of the blade allows for the calculation of time series for the strain components at any given blade location (*r*,*s*,*z*), i.e. through the thickness of the shell material (*r*), around the cross-section's perimeter (*s*) and along the beam's axial length (*z*). Similarly, corresponding time series for the stress components σ_{ij} (*r*, *s*, *z*; *t*), (*i*, *j* =1, 2) in the materials frame-of-reference can be obtained. At each blade location (*r*, *s*, *z*) a bivariate histogram f_σ (σ_a, σ_m; *r*, *s*, *z*) indicating the number of cycles occurring during the reference time frame for a given combination of mean stress σ_m and stress amplitude σ_a is calculated. A rainflow-counting algorithm [15], [22] has been adopted for this purpose. The following approach has been adopted for processing fatigue-induced degradation and damage at a given location (*r*, *s*, *z*):

1. A fixed reference interval for updating blade materials properties is defined. For typical 20-year fatigue evaluation period a 6-month reference interval was found to be sufficient to capture the (slow) degradation dynamics while still maintaining computing efficiency.

2. The wind resource information at the site of interest is classified by its mean wind speed for a given 10-min interval, leading to a normalized histogram f_U ($\overline{U}_{\infty,10}$). Each 10-min wind speed class can be associated with a triplet (ρ_v, $v_{\max}$,$v_{\min}$) which is obtained from averaging the corresponding values of the standard deviation, maximum and minimum wind speed for a given $\overline{U}_{\infty,10}$ class. In case the variation of these variables within a given $\overline{U}_{\infty,10}$ class is large, the $\overline{U}_{\infty,10}$-based classification can be replaced by a cluster analysis approach. In either case, a relatively small number of wind resource classes (typically, of order of 10-20) will result from this step.

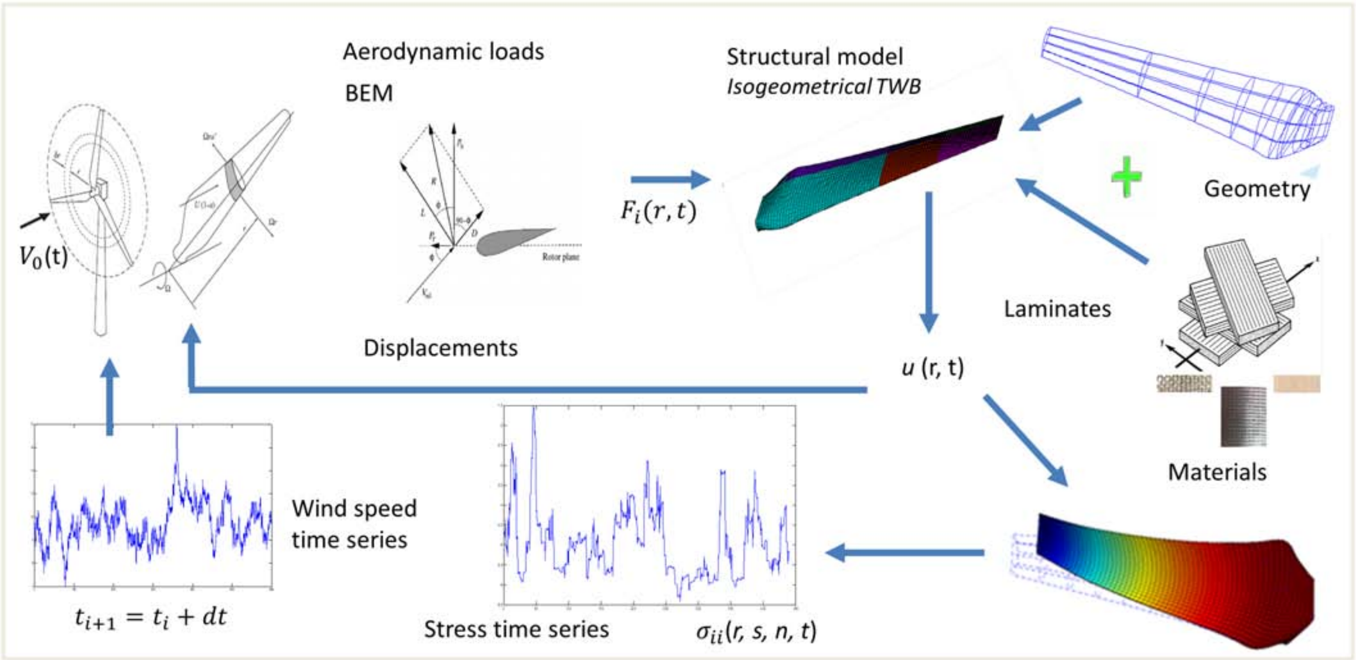

Figure 1 Graphic summary of the modeling process

3. Each wind resource class is associated with a time series generated from the four numbers ($\bar{U}_{\infty,10}$,ρ_v,$v_{\max}$,$v_{\min}$). For brevity, only $\bar{U}_{\infty,10}$ will be used to identify each class in the following. For each representative 10-min wind speed time series $U_{\infty,c}(t)$ corresponding stress time series $\sigma_{ij}(t; r, s, z; \bar{U}_{\infty,10})$ $(i, j=1,2)$ are calculated from the coupled (TWB-BEM) aeroelastic model.

4. Each stress time series σ_{ij} $(t; r, s, z; \bar{U}_{\infty})$ is subjected to a rainflow-type cycle counting algorithm providing a bivariate stress histogram $f_\sigma^{ij}(\sigma_a,\sigma_m; r, s, z; U_\infty)$ for each location (r, s, z) and wind resource class $\bar{v}_{10}$.

5. Stress histograms for a given location but different wind resource classes are combined into one after specifying suitable fixed σ_a, σ_m classes, leading to an average stress histogram $f_\sigma^{ij}(\sigma_a,\sigma_m;r, s, z)$.

6. A simplified stress histogram is obtained by setting suitable thresholds on both the values of (σ_a, σ_m), i.e.

$$f_\sigma^{ij}\left(\sigma_a,\sigma_m\right)=0 \quad \text{if} \quad \sigma_a<\sigma_{a,\text{tresh}} \vee \sigma_m<\sigma_{m,\text{tresh}}, \tag{19}$$

and the frequency of a given (σ_a,σ_m) class, i.e.

$$f_\sigma^{lj'}=0 \quad \text{if} \quad f_\sigma^{lj}<f_{\text{thresh}} \tag{20}$$

where the prime indicates the filtered histogram.

Local degradation of the materials strength is conducted at (r, s, z) according to the fatigue model described in section 2.2, where an equivalent cycle concept [17] has been used to concatenate fatigue blocks pertaining to different (σ_a, σ_m) classes. Omitting material indices $(i, j=1, 2)$ and coordinates (r, s, z) for readability, the equivalent number of fatigue cycles $n_{eq}^{(k)}$ after k previous fatigue blocks (each with a constant (σ_a, σ_m) pair) can be calculated in a recursive fashion from the requirement of the residual strengths S_r at the end of the k previous blocks and at the beginning of block k+1 to be equal:

$$S_r\left(n_{eq}^{(\kappa)},N_f\left(\sigma_a^{(\kappa+1)},\sigma_m^{(\kappa+1)}\right)\right)=S_r\left(n_\kappa+n_{eq}^{(k-1)},N_f\left(\sigma_a^{(\kappa)},\sigma_m^{(\kappa)}\right)\right), \tag{20}$$

In other words, $n_{eq}^{(k)}$ is the equivalent number of fatigue cycles after k previous blocks that would have caused the same degradation as the stresses $(\sigma_a^{(k+1)}),\sigma_m^{(k+1)})$ of block k+1 as n_k plus $n_{eq}^{(k-1)}$ equivalent cycles at stresses $(\sigma_a^{(k)})$, $\sigma_m^{(k)})$, or – equivalently – the complete fatigue history of the previous k blocks. The aforementioned idea is illustrated in the lower-left inset of Figure 2. The equivalent cycle concept [17] and, consequently, equation (19) are based on the assumption that strength degradation at a given constant stress pair (σ_a, σ_m)

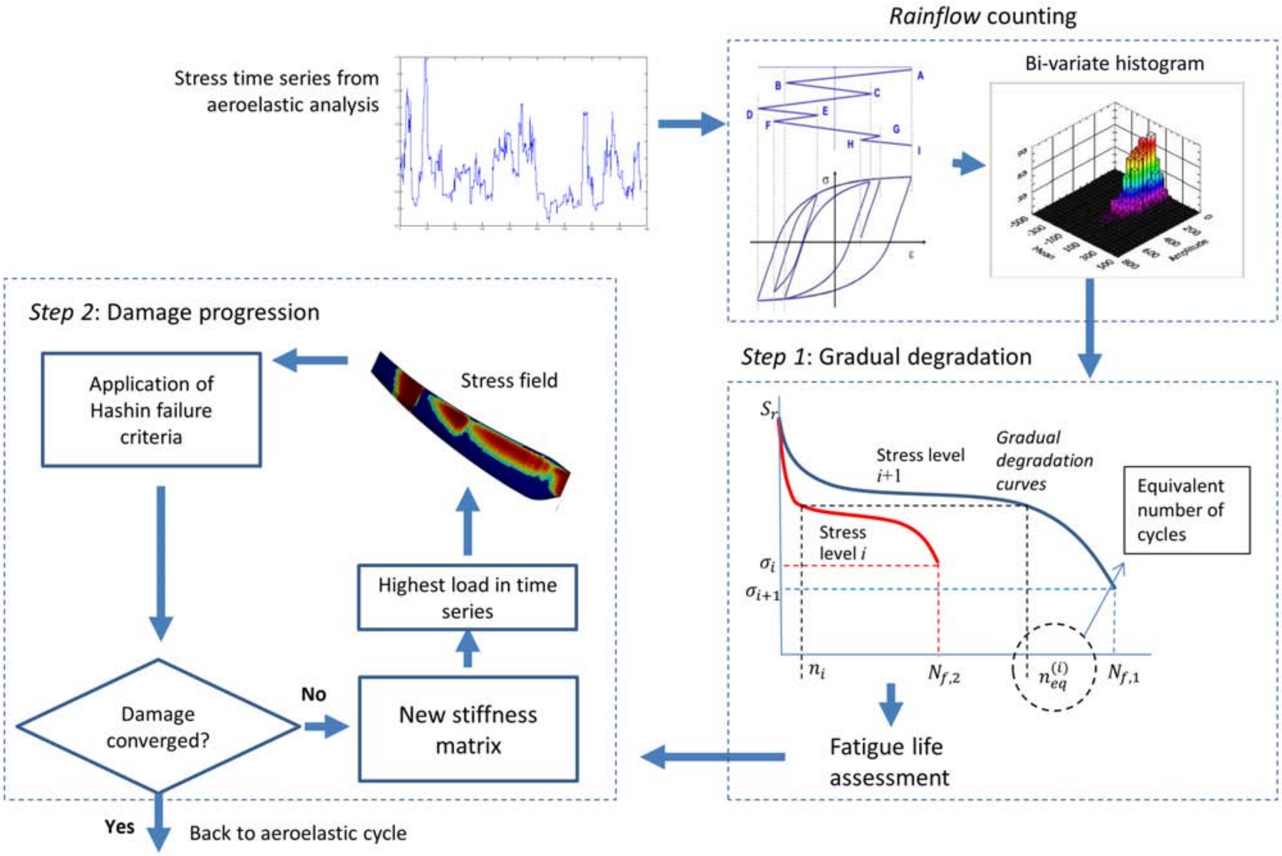

Figure 2 Pictorial description of two-step fatigue degradation and damage progression process

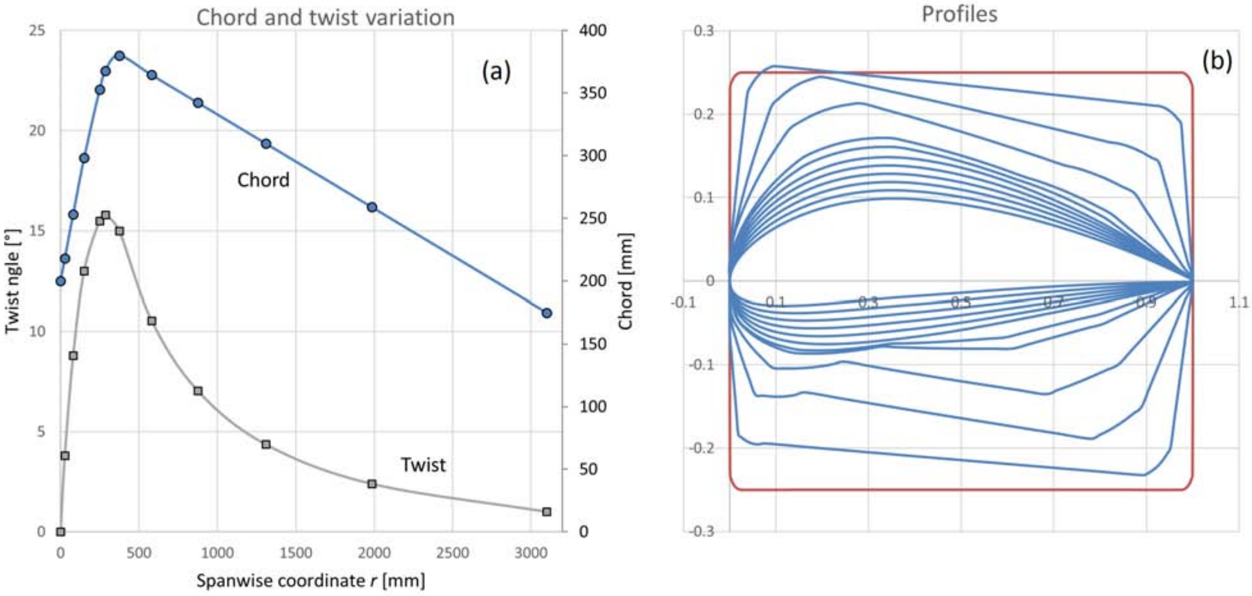

Figure 3 Outer geometry of the wind turbine blade analyzed in the present work. Left: Spanwise chord and twist angle variation. Right: Projected view of the normalized profiles

always occurs along a universal strength degradation curve for those stresses, where the curve is resumed at the point of residual strength.

Damage is assessed in two steps, indicated in Figure 2 and previously described in [12] for the case of a constant-amplitude load. The first step in the evaluation of the effects of a given fatigue stress block (σ_a, σ_m) is the identification of material cells having reached their fatigue life N_f, i.e. for which $S_r(n) \leq \sigma_{\max}$ for a given material direction. The materials properties of the affected cells are then degraded according to the rules given in [12], [16]. The second step involves a recursive process involving the self-consistent calculation of the stress field in the presence of the evolving fatigue damage field [12]. The failure criteria proposed by Hashin [24] are used to probe the additional damage incurred because of stress relocation, both within layers and between layers; see [12] for a detailed description.

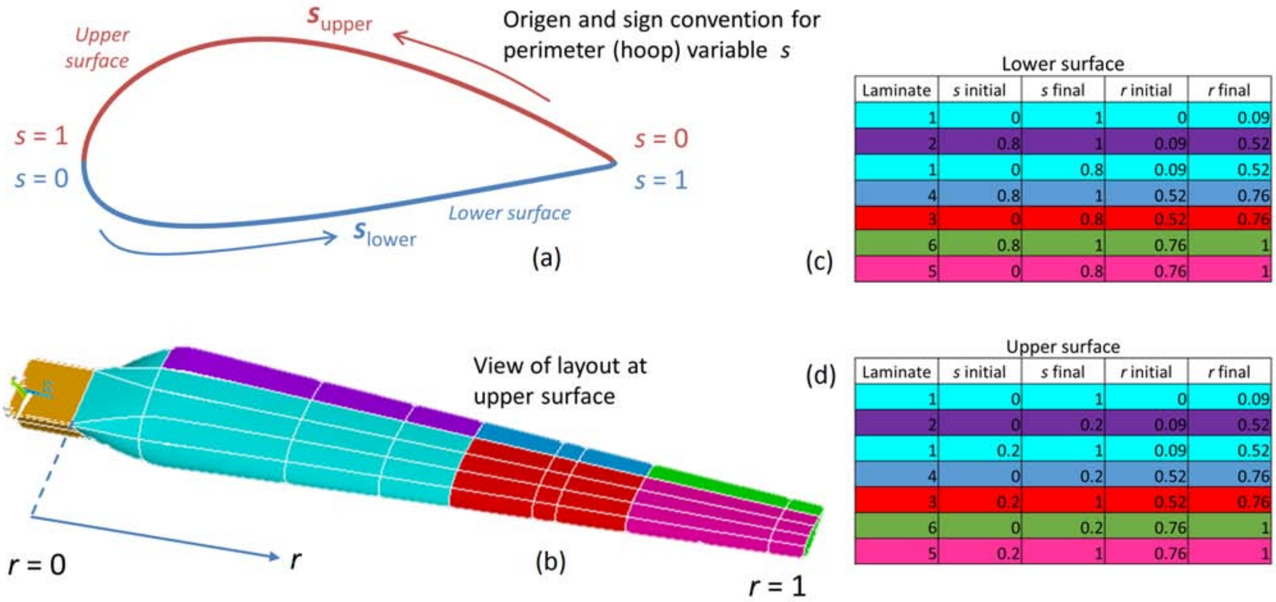

Lower surface

Laminate	*s* initial	*s* final	*r* initial	*r* final
1	0	1	0	0.09
2	0.8	1	0.09	0.52
1	0	0.8	0.09	0.52
4	0.8	1	0.52	0.76
3	0	0.8	0.52	0.76
6	0.8	1	0.76	1
5	0	0.8	0.76	1

Upper surface

Laminate	*s* initial	*s* final	*r* initial	*r* final
1	0	1	0	0.09
2	0	0.2	0.09	0.52
1	0.2	1	0.09	0.52
4	0	0.2	0.52	0.76
3	0.2	1	0.52	0.76
6	0	0.2	0.76	1
5	0.2	1	0.76	1

Figure 4 Material layup. (a) Conventions for the perimeter parameter s. (b) Upper side of turbine blade showing the different laminates. (c) Table with the confines of each laminate (upper surface). (d) Table with the confines of each laminate (lower surface)

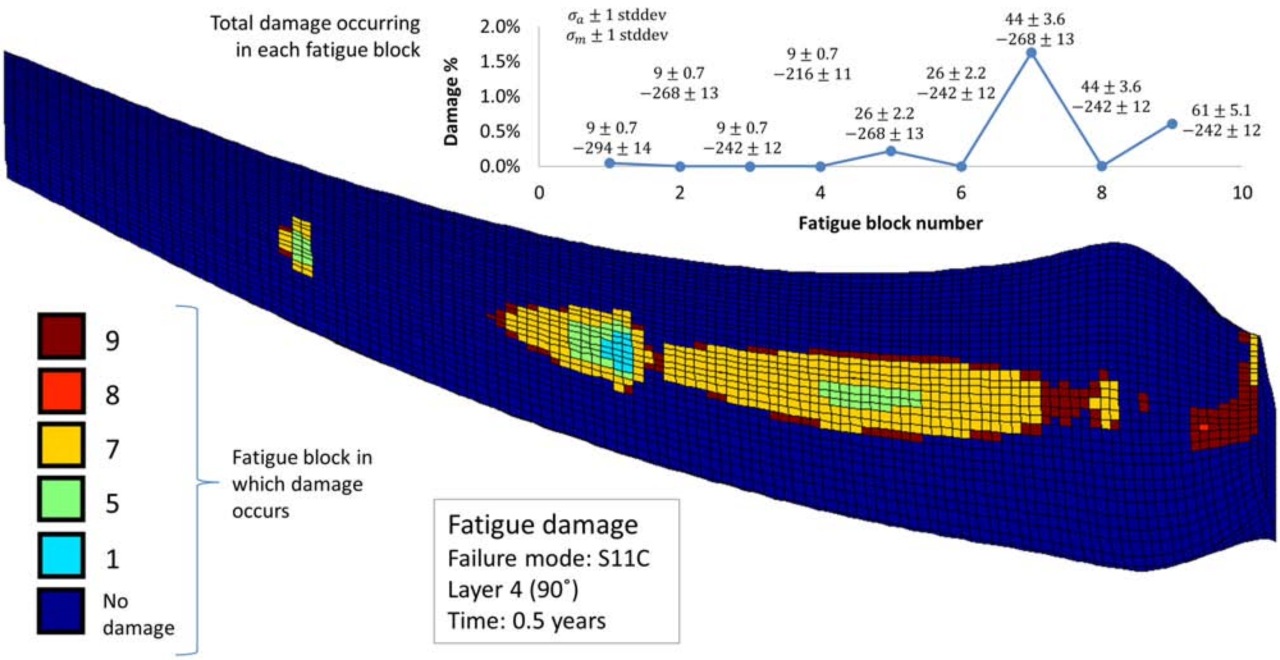

Figure 5 Fatigue damage occurred after 0.5 years of exposure in layer 4 on the lower side of the blade because of fiber compression failure (first step of the damage progression assessment). Inset: Total damage occurring in each of the fatigue blocks

Description of case study

A blade of a prototype 10 kW wind turbine built from unidirectional composite material with a total length of 3.5m was used as a numerical study case. The outer geometry is shown in Figure 3, while the material layup is described in Figure 4. The properties of the laminates are given in Table 2. Stiffness and strength values were obtained from the manufacturer, while fatigue degradation parameters were taken from Shokrie [16]; see Table 1.

A stochastic wind speed time series for a 10-min interval with specified values of the mean, gust, anti-gust wind speed, and standard deviation was generated according to Section 2.3(a). Local stress time series for all modeled material degrees of freedom (along the fiber, perpendicular to the fiber, shear) at all locations (*r, s, z*) were calculated from the coupled aeroelastic model as described in Sections 2.1 and 2.3(b). Cycle counting and strength degradation calculations were performed according to Section 2.3. As there is no conceptual difference in the treatment of a situation for a constant average wind speed ($f_v = \delta(\overline{U}_{\infty,10} - \overline{U}^{(0)}_{\infty,10})$) and a realistic $\overline{U}_{\infty,10}$ wind speed distribution (say, a Weibull distribution) in the framework of the present work (see Section 2.3), a δ-shaped $\overline{U}_{\infty,10}$ wind speed distribution was used for the case study. A systematic assessment of the effect of the wind resource on fatigue degradation and blade design will be conducted in follow-up work.

Similarly, ideally correlated wind speed times series over the rotor disk were assumed over the swept rotor area, which is a reasonable assumption given the small rotor size. In larger rotors, such as the ones used in modern multi-MW wind turbines the finite spatial correlation over the rotor disk, resulting in rotational sampling effects, has to be taken into account. These effects will be addressed in follow-up work. Fatigue life assessments were conducted in half-year intervals, followed by their recursive respective damage progression evaluation based on recalculation of the stress field and the application of the Hashin criteria (step 8 in Section 2.3).

Initial strength and stiffness			*Stiffness and strength degradation parameters*				*Fatigue life parameters*	
Failure mode	Initial stiffness *E* [Gpa]	Initial strength *S* [Mpa]	λ	γ	α	β	*A*	*B*
11T	147	820	14.57	0.3024	10.03	0.473	1.3689	0.1097
11C	10'	450			49	0.025		
22T	8.87	45	14.77	0.1155	9.6287	0.1255	0.999	0.096
22C	10.1	175			67.36	0.0011		
12	5.0	137	0.7	11	0.16	9.11	0.099	0.186

Table 1 Elastic, strength and fatigue parameters of the adopted fatigue model. Degradation and initial stiffness parameters are from Shokrie [19]

Layer	Thickness [mm]				Angle [°]	Thickness [mm]		Angle [°]
	Laminates					Laminates		
	1	2	3	5		4	6	
1	0.25	0.2	0.2	0.1	0	0.5	0.3	90
2	0.25	0.2	0.2	0.1	45	-	-	-
3	0.25	0.2	0.2	0.1	-45	-	-	-
4	0.5	0.4	0.4	0.2	90	-	-	-
5	0.25	0.2	0.2	0.1	-45	-	-	-
6	0.25	0.2	0.2	0.1	45	-	-	-
7	0.25	0.2	0.2	0.1	0	-	-	-

Table 2 Lamination sequence for all laminates; laminates 4 and 6 correspond to trailing edge portions at the mid-blade and tip section and only have one layer. The angles of the unidirectional composite layers indicated in column 6 are with respect to the hoop direction.

Results and discussion

Damage propagation – fatigue life and damage progression

Figure 5 shows a map, overlain on a three-dimensional rendering of the blade, of the damage occurring in layer 4 after half a year of operation as the nine fatigue blocks obtained from rainflow analysis of the stress field at each of the material cells are applied consecutively, where damage is measured as the percent of the total material cells which already reached their associated fatigue life (i.e. failed). The average values and the standard deviations of both σ_m and σ_a in each block have been indicated in the upper graph of Fig. 5, which also shows the damage due to cells reaching their fatigue life according to the equation (5), i.e. those cells complying with $S_r(n)=\sigma_{\max}$. Fatigue life damage is solely due to compression and can be seen to occur in the root and the mid-blade section of layer 4, the one carrying most of the compressive load. The same stiffness matrix is used for all fatigue blocks, i.e. damaged cells are not removed from the stress field calculation until the next step of the damage progression procedure where the Hashin failure criteria are evaluated.

Once material cells having reached their fatigue life have been identified their structural properties are degraded according to the rules described in Shokrie [16]. Consequently, stress shifts to either adjacent areas or other layers, exposing other material cells to potential damage. This is assessed in the second step of the damage assessment process, the damage propagation step based on recursive calculation of the stress field and the application of the Hashin failure criteria. The results for the case of the damage evaluation after 0.5 years are shown in Fig. 6. It can be seen that additional damage occurs in the vicinity of the pre-existing fatigue damage, initiating right at the edge of the existing damage zone and progressing outwards. The stiffness matrix is updated after each iteration, and the stress field is re-calculated consequently. The damage propagation process in Figure 6

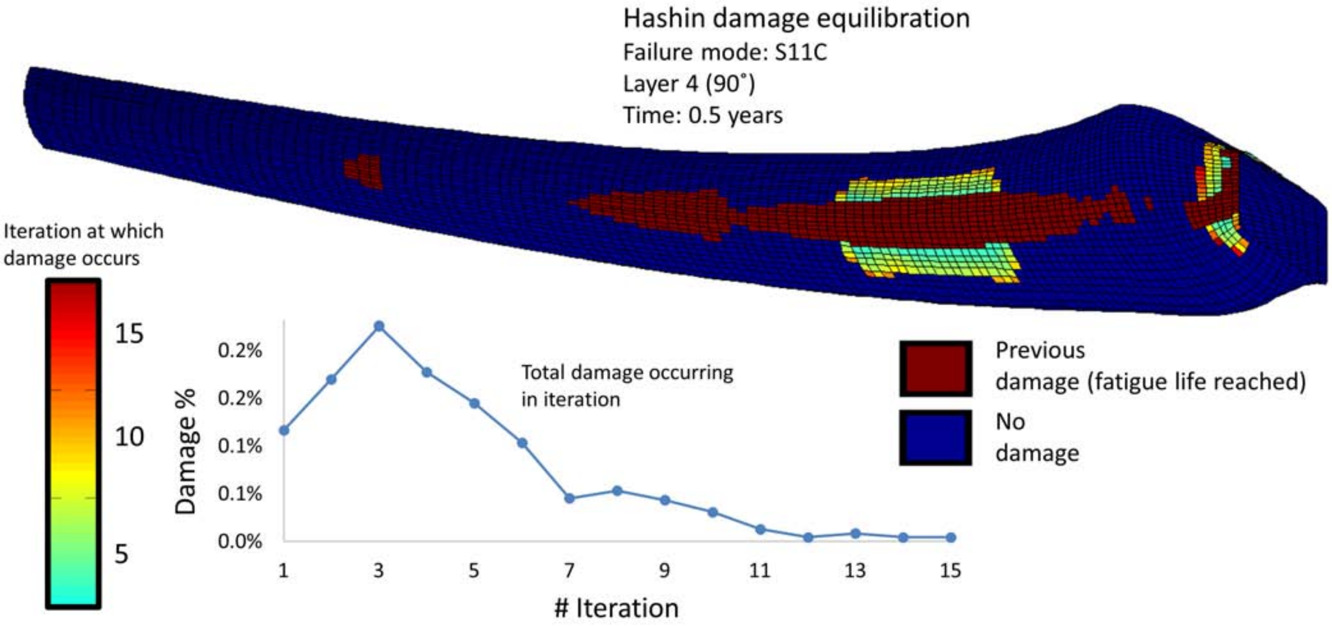

Figure 6 Damage progression occurring after 0.5 years on the lower side of the blade because of fiber compression failure in layer 4 (second step of the damage progression assessment). Inset: Total damage occurring in each of the iterations

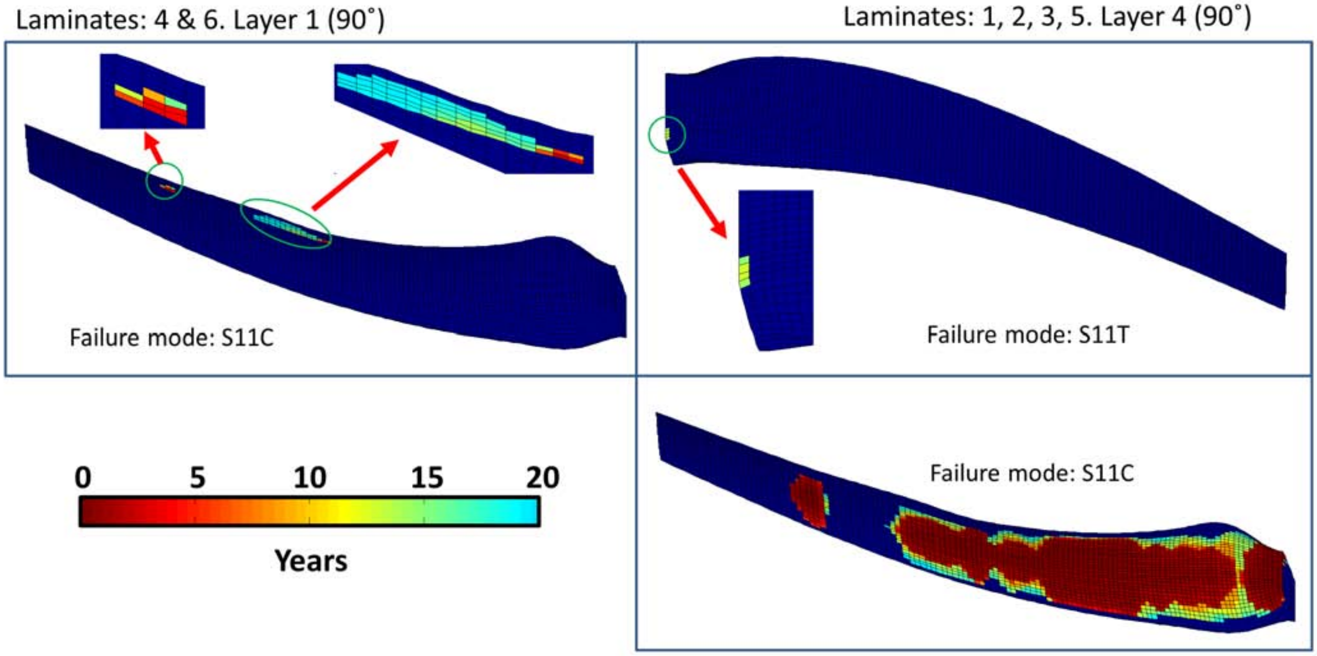

Figure 7 Total damage after 20 years of exposure in different parts of the blade due to failures in the fiber (both tension and compression). The colors code for the time in which damage in a specific zone occurs.

can be seen to converge after about 15 iterations. This second step of damage progression is a consequence of a redistribution of the stress field within layer 4 combined with a strongly reduced residual strength of the material cells in the vicinity of the original damage zone.

Damage accumulated during the operational lifetime

Once some of the basic mechanisms governing the fatigue damage propagation have been identified it is instructive to inspect how damage progresses over the lifetime of the blade throughout its geometry. Figures 7 and 8 show damage occurring both in the main laminate sections (1, 2, 3, and 5) as well the trailing edge laminates 4 and 6 (see Fig. 4). Not unexpectedly, compression damage is the predominant failure mode at the downwind side of the blade as it withstands a strong constant axial force making it more vulnerable to the oscillating component of the load. As layer 4 carries most of the compression load, it also takes most of the damage, most of which occurs in the early years and afterwards progresses only moderately. Similarly, tensile damage occurs at the upwind side, with the predominant failure mode being matrix failure (label S22T in Fig. 7). While layers oriented at 90° which respect to the hoop carry a higher portion of the tensile load the tensile strength is also far higher (S11T >> S22T), keeping 90°-oriented layers from being damaged. Shear failure is another of the main failure modes and is associated with 45°-oriented layers located on the compressive side of the blade, where the axial wind force produces also some shear stress. Most of the corresponding damage occurs in the region suffering from Hashin degradation due to compression failure and the corresponding loss of compression-load carrying capacity, which contributes to activating the Hashin criterion for shear failure.

Evolution of damage progression by failure mechanism

A summary of the failure mechanisms acting on the blade during its lifetime is provided in Figure 9. The left subfigure shows the progression of damage by failure mechanism, whereas the right subfigure also provides the split-up of the total damage recorded on account of a given failure criterion between fatigue-life and Hashin. As evidenced by Figure 9 initial damage occurs early on in the blade's life, with a total of 7% damage occurring in the first year of operation due to fiber compression failure (curve labelled S11C).

As shown in Figures 5 and 6 this damage predominantly occurs at the root section of the downwind side of the blade which is subjected to a constant average compression with an average stress before failure in the range of 240-270 MPa and an amplitude of the variable component of up to 40-60 MPa. The damage is confined to layer 4, as this layer carries most of the load. Other layers, given their orientations, have lower resistance to compression but they also carry much lower stresses. While the initial fiber compression strength of 450 MPa is large enough to withstand these stresses in a new blade, the strength degradation occurring over the course of the first year of operation is large enough to push the remaining strength of the central part of the root section and a (smaller) central mid-blade region below the acting maximum stress. Once the initial failure has occurred, adjacent material cells become exposed to further damage as probed by the Hashin criterion. As mentioned before, shear failure occurs (in 45°-oriented layers) soon (around year 3) after the compressional load-carrying capacity in layer 4

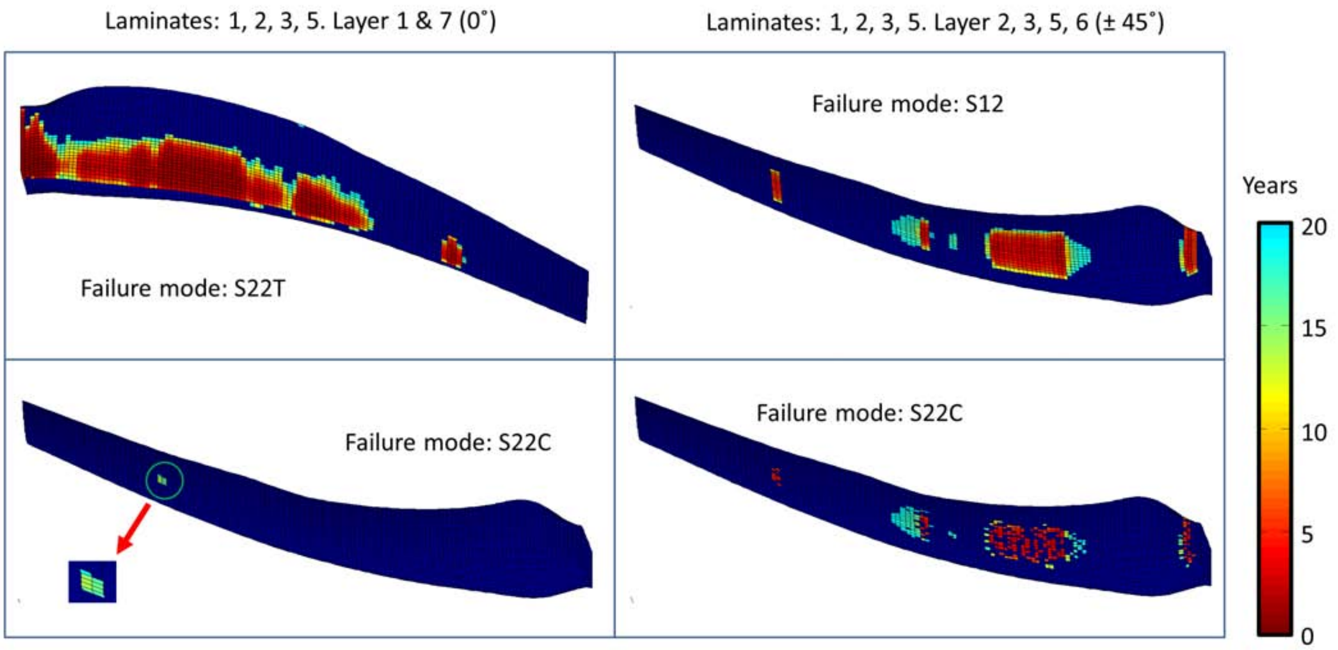

Figure 8 Total damage after 20 years of exposure in different parts of the blade, due to matrix (both tension and compression) and shear failure. The colors code for the time in which damage in a specific zone occurs

has been partly compromised, leading to an increase of the compressional stress term to the Hashin shear failure criterion. As evidenced by the large gap between fatigue-life induced and total shear failure most of the shear damage is due to this mechanism. The last important failure mechanism, matrix tensile failure (label S22T), can be seen to evolve continuously with all damage being due to cells reaching their fatigue life, with no further damage propagation due to stress re-allocation and interaction between stress components.

Impact of damage progression on blade stiffness

The effect of the fatigue-induced degradation on the overall elastic properties of the blade over time is shown in Fig. 10 where the displacements along three of the global degrees of freedom (u_{flap}, u_{edge}, φ), i.e. flapwise (u_{flap}, in the direction of the free-stream wind velocity), edgewise (*u*edge, within the rotor plane), and torsional displacement (φ, around the blade axis), have been plotted as a function of the spanwise blade coordinate, normalized to the tip displacement for the

Edición digital

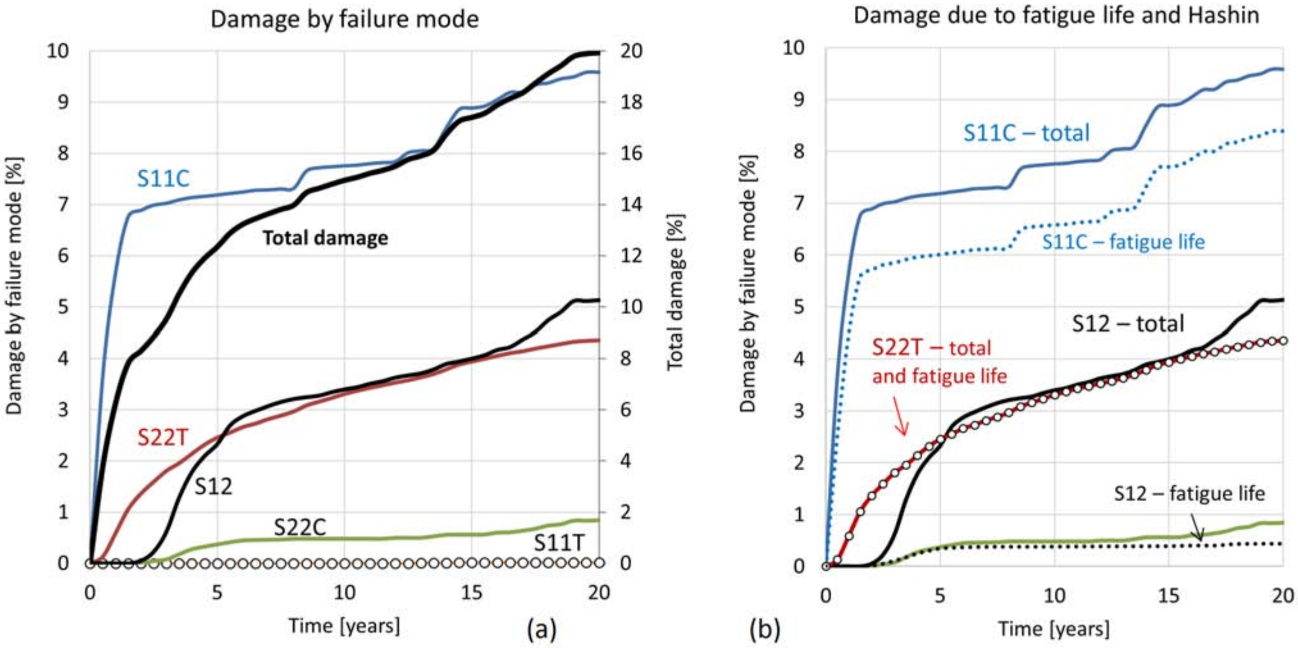

Figure 9 Damage resolved by failure mode and mechanism (fatigue life / Hashin) as a function of time. Left: Damage by failure mode and total damage. Right: Damage by failure mode and mechanism, excluding fiber tension failure

undamaged blade. A unit load in each of the degrees of freedom has been placed at the tip for each case. The derivative of each function was added to reveal finer details.

As shown in Figure 10, fatigue-induced degradation translates into a relatively uniform softening in the flapwise and edgewise degrees of freedom, with an 80% increase in flapwise displacement of the blade tip after 20 years of operation, compared to about 50% for the edgewise motion. While $\mathrm{d}\,u_{\mathrm{edge}}/\mathrm{d}z$ is largely featureless, the flapwise derivative displays some structure providing information of the underlying degradation mechanisms. It is conspicuous that the undamaged blade shows a discontinuity in $\mathrm{d}\,u_{\mathrm{flap}}/\mathrm{d}z$ at a radial position of about 2400mm, which can be related to the change in material layup occurring at 76% of the effective elastic blade radius of 3100mm (see Fig. 4). Here, the total thickness of the 7-layer laminate changes from 1.6mm to 0.8mm, evidently reducing the local stiffness. After 20 years of operation, the discontinuity in $\mathrm{d}\,u_{\mathrm{flap}}/\mathrm{d}z$ significantly steepens right at the transition between laminates, but no effect on $\mathrm{d}\,u_{\mathrm{flap}}/\mathrm{d}z$ is observed further down the blade, indicating that the softening effect is confined to the transition region.

These findings are fully consistent with the damage maps in Figures 7 and 8, showing a significant amount of fatigue damage in the transition region, most of it occurring early on in the blade's operational lifetime. Referring to the second feature in $\mathrm{d}\,u_{\mathrm{flap}}/\mathrm{d}z$, a steep rise at a radial position of about 1650mm, it can be seen that this position again coincides with the discontinuity in material layup from laminate 1 to 3 at 52% of the blade radius. As laminate 1 is only 20% thicker than laminate 3 no apparent change in $\mathrm{d}\,u_{\mathrm{flap}}/\mathrm{d}z$ shows up in the undamaged blade. As shown in Figures 7 and 8, however, there is a considerable amount of fatigue damage in this zone, with early fibre compression failure occurring in layers 1, 2, 3, and 5, followed by matrix compression and shear failure towards the year 20. The feeble features in the $\mathrm{d}\,u_{\mathrm{edge}}/\mathrm{d}z$ curves at r = 52% and 76% show that edge stiffness is much less affected. The main reason for this lies with the fact that fatigue mostly affects layers with fiber orientations along the blade axis (or at 90° to the hoop direction), given the predominant action of the stresses in this direction. Therefore, hoop-oriented layers are less degraded, and consequently the edgewise stiffness is less affected.

Regarding the time evolution of the damage, it is evident from Figure 10 that the fingerprint of the damage progression process is very similar in the flap- and edgewise coordinates, with step changes occurring in distinct moments in time. The structure of the torsional evolution curve, however, can be seen to be substantially different. Given the sturdy structure of the root section for $r \leq 52\%$ practically no torsional deformation occurs, both at the original and the fatigue-damaged blade. At the transition to the mid-blade section a quite dramatic impact on torsional stiffness can be observed, as evidenced by the evolution of the $\mathrm{d}\varphi/\mathrm{d}z$-feature at 52% from a shoulder for the undamaged blade to a distinctive peak after 18.5 years and an additional strong rise in peak amplitude after 20 years. Similarly, at the 76% transition a distinctive feature can be observed, but the change from a shoulder to a peak does not occur until 20 years of operation. The reason for the strong reduction in torsional stiffness at the 52% transition becomes obvious if we observe that the blade section between 52% and 76% has a

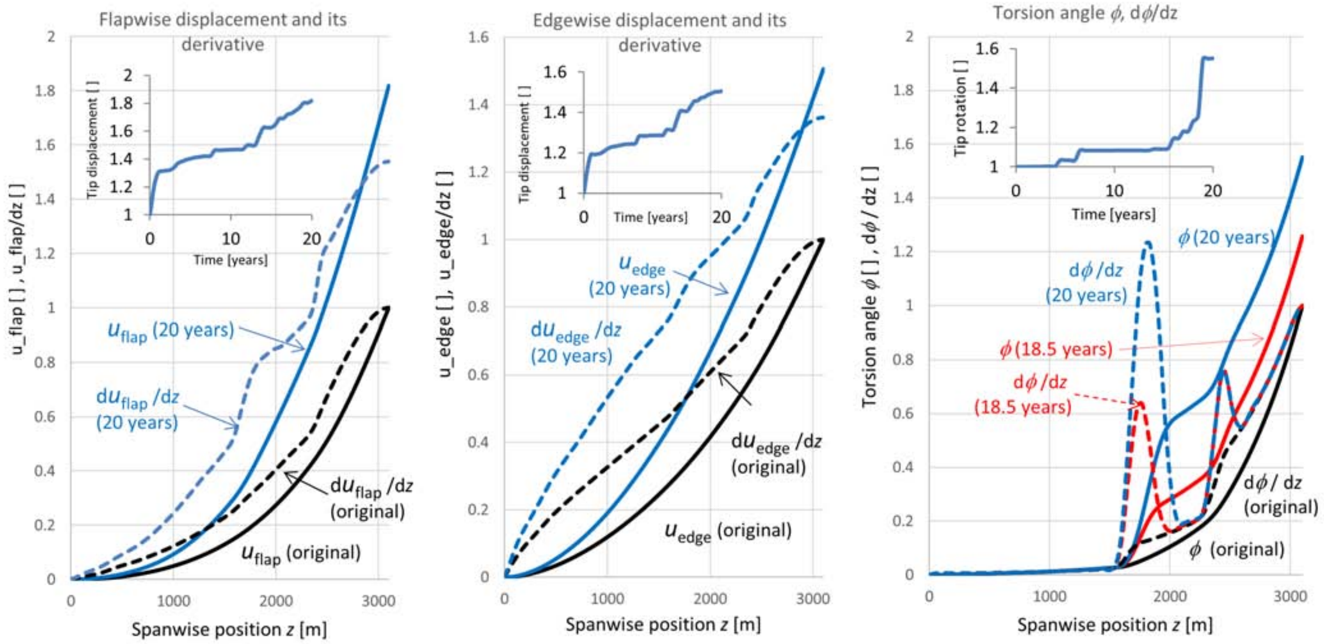

Figure 10 Displacement curves for the flapwise, edgewise, and rotational degrees of freedom as a function of the spanwise (radial) position for the undamaged blade and after 20 years of fatigue exposure. A unit load in the corresponding degree of freedom was placed at the tip in all cases. Displacements and their derivatives are normalized to their values for the undamaged blade. Insets: Tip displacement (flapwise, edgewise, and torsion, respectively) as a function of time.

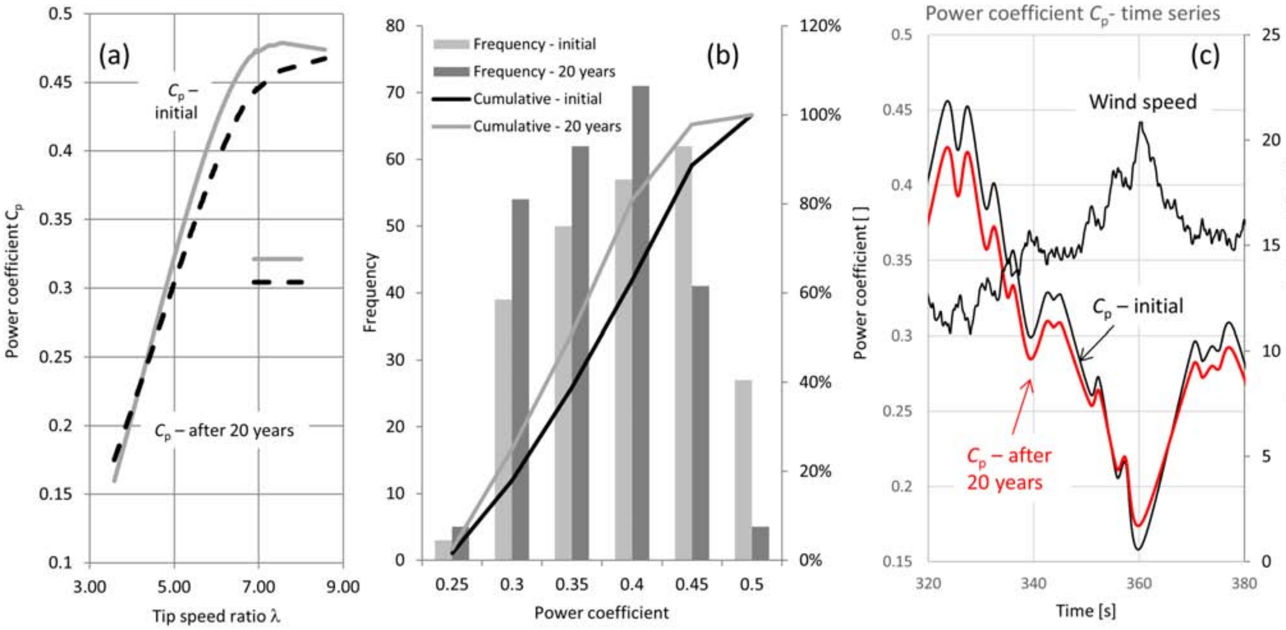

Figure 11 Change in aerodynamics due to fatigue-induced aging during 20 years. (a) C_p(power coefficient) vs. λ (tipo speed ratio). (b) Distribution of C_p operating points. (c) Time series C_p in the vicinity of a wind speed gust.

trailing edge termination consisting of one laminate layer only, as opposed to the rest of the blade which boasts seven layers of laminates. The reason for this reduction evidently lies with the small dimension of the trailing edge region in the mid-blade section, making this section especially vulnerable. It can be seen from Figure 7 that this part of the blade suffers from some initial fiber compression damage in the early years of operation, with a substantial increase in damage occurring around the year 15, with the subsequent growth of a crack in the years 15 through 20. As the torsional stiffness essentially relies on the structural integrity of the hoop, and the hoop in this region relies on one layer only, a crack in this layer evidently leads to a dramatic increase in torsional bending. A similar process occurs at the 76% transition, but the damage remains confined to a small area.

As a final illustration of the capabilities of the novel integrated fatigue damage progression methodology for wind turbine blades and other rotary machinery the impact of fatigue damage on the aerodynamic properties of the blades will be briefly discussed. Figure 11 (a) shows the C_p-λ (power coefficient vs tip speed ratio) curve both for the new rotor and after 20 years of operation. It can be seen that a reduction of about 2-3% in power is observed in the vicinity of the design tip speed ratio; the stall regime (corresponding to smaller values) is less affected. Figure 11 (b) demonstrates the effect on energy production by plotting the C_p distributions for the new and the aged rotor; the shift of the distribution to smaller value is clearly conspicuous. Figure 11(c) shows a 10-min wind speed time series together with the corresponding time series for the power coefficient of the stall-regulated wind turbine. Due to the relatively high wind speed (averaging 14 m/s) and the stall regulation scheme the power coefficient responds directly to the variations in wind speed. Stall regulation results in higher axial wind loads than pitch regulation and consequently in higher fatigue damage; a systematic assessment of the effect of different regulation schemes on the initiation and propagation of fatigue damage can be conveniently studied with the current methodology and will be addressed in follow-up work.

Not unexpectedly, as shown in Figure 11, the degraded blade has a somewhat poorer aerodynamic performance compared to the new blade, particularly at relatively low wind speeds or high C_p values where a reduction of several percent can be observed, which directly translates into lower energy capture. At high wind speeds (or low C_p values, given the stall regulation) the new and the degraded blade behave quite similarly (see the close-up of the gust event in Figure 11(c)). This differentiated effect of fatigue degradation on blade aerodynamics was somewhat expected as near the optimal aerodynamic point of operation the flow conditions are quite sensitive to small rotations of blade sections whereas under fully developed stall conditions (such as at *t*=360s in Figure 11(c)) there is little sensitivity to the details of the blade geometry. A more detailed assessment of impact of fatigue aging on rotor aerodynamics will be covered in follow-up research.

Summary and conclusions

A novel methodology for the continuous assessment of fatigue damage propagation in wind turbine blades subjected to stochastic wind loads has been presented. The new tool was built around an aeroelastic model based on Thin-Walled Beam (TWB) and Blade Element Momentum (BEM) theories, complemented with an integrated fatigue damage assessment and propagation model designed to handle stochastic stress time series. It was demonstrated how the proposed approach is capable of tracking the initiation and propagation of fatigue damage over large time periods such as the typical lifetime of a wind turbine blade, allowing to study its impact on the mechanical properties of the blade. Applications of the proposed methodology include the design of turbine blades with smaller safety factors and hence less material, leading to lighter and less expensive blades, faster design and optimization cycles, the study of different wind turbine control algorithms, and the design of structural health monitoring systems.

Acknowledgments

Support from the School of Engineering and Sciences at Tecnológico de Monterrey and the Mexican Center for Innovation in Wind Energy (CEMIE Eólico) through project P19 are gratefully acknowledged.

References

[1] Brøndsted, P. and Nijssen, R.P.L., '*Fatigue as a design driver for composite wind turbine blades*', in Brøndsted, P. and Nijssen, R.P.L. (Ed.): '*Advances in wind turbine blade design and materials*' (Woodhead Publishing Limited, 2013), pp. 175-209

[2] Burton, T., Sharpe, D., Jenkins, N.; Bossanyi, E. '*Wind energy handbook*' (John Wiley and Sons, Inc. 2001) pp. 209–328

[3] Leku, D.J. ' *Probabilistic design of wind turbine blades*', in Brøndsted, P. and Nijssen, R.P.L. (Ed.): '*Advances in wind turbine blade design and materials*' (Woodhead Publishing Limited, 2013), pp. 325 – 359

[4] Shokrieh, M.M., and Rafiee, R. '*Simulation of fatigue failure in a full composite wind turbine blade*'. Composite Structures, 2006, 74, (3), pp 332 – 342.

[5] Lee, C. S., Kim, J. H., Kim, S. K., Ryu, D. M., & Lee, J. M. '*Initial and progressive failure analyses for composite laminates using Puck failure criterion and damage-coupled finite element method*'. Composite Structures, 2015, 121, pp 406 – 419.

[6] Nikishkov, Y., Makeev, A., Seon, G. '*Progressive fatigue damage simulation method for composites*'. International Journal of Fatigue, 2013, 48, pp 266 – 279

[7] Cárdenas, D., Elizalde, H., Marzocca, P., Abdi, F., Minnetyan, L., & Probst, O. '*Progressive failure analysis of thin-walled composite structures*'. Composite Structures, 2012, 95, pp 53 – 62

[8] Pawar, P. M., Ganguli, R. '*Modeling progressive damage accumulation in thin walled composite beams for rotor blade applications*'. Composites Science and Technology, 2006, 66, (13), 2337 – 2349.

[9] Librescu, L., Song, O. '*Thin-walled composite beams: theory and application*'. (Springer Science & Business Media, 2006).

[10]'*GENOA Virtual Testing & Analysis Software*', http://www.ascgenoa.com/, accessed 30 March 2016

[11] Cárdenas, D., Elizalde, H., Marzocca, P., Gallegos, S., Probst, O. '*A coupled aeroelastic damage progression model for wind turbine blades*'. Composite Structures, 2012, 95, pp 3072–3081

[12] Rivera, J.A., Aguilar, E., Cárdenas, D., Elizalde, H., Probst. O. '*Progressive failure analysis for thin-walled composite beams under fatigue loads*'. Composite Structures, 2016, 154, pp 79–91

[13] Shokrieh, M. M., Lessard, L. B. '*Progressive fatigue damage modeling of composite materials, Part I: Modeling*'. Journal of Composite Materials, 2000, 34, (13), 1056-1080.

[14] Zhang, Y. X., & Yang, C. H. '*Recent developments in finite element analysis for laminated composite plates*'. Composite Structures, 2009, 88 (1), 147–157.

[15] Talreja, R., & Singh, C. V. '*Damage and failure of composite materials*' (Cambridge University Press, 2012)

[16] Shokrieh M. M. '*Progressive fatigue damage modeling of composite materials*'. PhD thesis, McGill University, 1996.

[17] Nijssen, R. P. L. '*Fatigue life prediction and strength degradation of wind turbine rotor blade composites*', PhD thesis, Delft University of Technology, 2006

[18] Jang, Y.J, Choi, C.W., Lee J.H., Kang, K.W. '*Development of fatigue life prediction method and effect of 10-minute mean wind speed distribution on fatigue life of small wind turbine composite blade*'. Renewable Energy, 2015, 79, pp 187-198

[19] Montesano, J., Chu, H., Singh C.V. '*Development of a physics-based multi-scale progressive damage model for assessing the durability of wind turbine blades*'. Composite Structures, 2016, 141, pp 50–62

[20] Vo, T. P., Lee, J. '*Flexural-torsional behavior of thin-walled closed-section composite box beams*'. Engineering Structures, 2007, 29, (8), 1774–1782

[21] Zhang, C., Wang, S. '*Structure mechanical modeling of thin-walled closed-section composite beams, Part 1: Single-cell cross section*'. Composite Structures, 2014, 113, pp 12-22.

[22] Harris, B. '*Fatigue in composites. Science and technology of the fatigue response of fibre reinforced plastics*' (Woodhead Publishing Ltd., 2003)

[23] Adam, T., Gathercole, N., Reiter, H., et al., '*Life prediction for fatigue of T800/5245 carbon fibre composites: II-Variable amplitude loading*', International Journal of Fatigue, 1994, 16, pp. 533-547

[24] Hashin, Z., '*Failure Criteria for Unidirectional Fiber Composites*', Journal of Applied Mechanics, 1980, 47, pp 329-334.

[25] J. Amezcua, J., Muñoz, R., Probst, O. '*Reconstruction of gusty wind speed signals from data logger time series*', Wind & Structures 2011, 14, (3), pp 337-357

[26] Martínez J., Bernabini, L., Probst, O., Rodríguez, C. '*An Improved BEM Model for the Power Curve Prediction of Stall-regulated Wind Turbines*', Wind Energy 2005, 8, pp 385-402